

Cite this: *Mater. Horiz.*, 2018,
5, 429Received 30th January 2018,
Accepted 26th February 2018

DOI: 10.1039/c8mh00128f

rsc.li/materials-horizons

A supramolecular hybrid material constructed from graphene oxide and a pillar[6]arene-based host–guest complex as an ultrasound and photoacoustic signal nanoamplifier†

Guocan Yu,^{‡a} Jie Yang,^{‡b} Xiao Fu,^{‡a} Zhantong Wang,^a Li Shao,^b
Zhengwei Mao,^{*c} Yijing Liu,^a Zhen Yang,^a Fuwu Zhang,^a Wenpei Fan,^a
Jibin Song,^{‡a} Zijian Zhou,^a Changyou Gao,^c Feihe Huang^{‡b} and
Xiaoyuan Chen^{‡a*}

Photoacoustic imaging combines the merits of ultrasound imaging and optical imaging, and allows a fascinating imaging paradigm with deeper tissue penetration than optical imaging and higher spatial resolution than ultrasound imaging. Herein, we develop a supramolecular hybrid material composed of graphene oxide (GO) and a pillar[6]arene-based host–guest complex (CP6⊃PyN), which can be used as an ultrasound (US) and photoacoustic (PA) signal nanoamplifier. Triggered by the near-infrared (NIR) light mediated photothermal effect, CO₂ nanobubbles are generated on the surface of GO@CP6⊃PyN due to the decomposition of the bicarbonate counterions, thus strongly amplifying its US and PA performances. Our study, for the first time, demonstrates enhanced US and PA activity in a supramolecular hybrid material on the basis of host–guest chemistry as a photoacoustic nanoplatform.

Photoacoustic (PA) imaging depends on the detection of ultrasonic waves generated by thermo-elastic expansion, and combines the advantages of both ultrasound and optical imaging.^{1–3} Compared with most optical imaging techniques, PA imaging provides extraordinary opportunities for monitoring and detecting disease pathophysiology *in vivo* benefiting from its capacity for high-resolution imaging of rich optical contrast at depths beyond the optical transport mean-free-paths. Efficient contrasts are urgently needed for excellent-performance PA imaging, in which the PA

Conceptual insights

As an emerging non-invasive diagnostic modality, photoacoustic (PA) imaging integrates the excellent tissue penetration of ultrasound (US) and high sensitivity of optical imaging, which provides extraordinary opportunities for detecting and monitoring disease pathophysiology *in vivo*. Superior contrasts with high optical-to-acoustic conversion efficiency are urgently needed to improve the performance of PA imaging, in which the PA agents can effectively convert the absorbed light to localized volume heating, thus resulting in transient thermoelastic expansion and consequently broadband acoustic waves. Unfortunately, thermoelastic expansion, which is the least efficient mechanism, is the main obstacle inhibiting the clinical application of PA imaging. Herein, we develop a novel supramolecular hybrid material (GO@CP6⊃PyN) fabricated from graphene oxide (GO) and a pillar[6]arene-based host–guest complex (CP6⊃PyN) by hierarchical self-assembly to solve this scientific issue. Carbon dioxide nanobubbles are generated *in situ* due to the decomposition of bicarbonate counterions triggered by the NIR light-mediated photothermal effect of GO, and can be used as “molecular boosters” to significantly enhance the US/PA signal amplitudes through thermoelastic expansion. This supramolecular strategy possessing the ability to change the fate of existing nanomaterials opens new opportunities for the construction of new and excellent imaging agents, showing irreplaceable advantages in theranostics.

signal amplitude is determined by the optical-to-acoustic conversion efficiency, including the light absorption and the conversion from absorbed laser energy to an outgoing thermoacoustic wave.^{4–6}

Due to their unique chemical, physical and mechanical properties, graphene and its derivatives have attracted tremendous interest for applications ranging from energy, electronics, and materials science to biomedicine. Among various graphene derivatives, graphene oxide (GO) has been extensively studied in biomedical applications such as bioassays, biosensors and drug delivery, arising from its easy preparation, high water solubility, excellent biocompatibility, low toxicity and ultrahigh drug loading efficiency.^{7–10} For example, GO has been widely utilized as a drug

^a Laboratory of Molecular Imaging and Nanomedicine, National Institute of Biomedical Imaging and Bioengineering, National Institutes of Health, Bethesda, Maryland 20892, USA. E-mail: shawn.chen@nih.gov

^b State Key Laboratory of Chemical Engineering, Center for Chemistry of High-Performance & Novel Materials, Department of Chemistry, Zhejiang University, Hangzhou 310027, P. R. China. E-mail: fhuang@zju.edu.cn

^c MOE Key Laboratory of Macromolecular Synthesis and Functionalization, Department of Polymer Science and Engineering, Zhejiang University, Hangzhou 310027, P. R. China. E-mail: zwmao@zju.edu.cn

† Electronic supplementary information (ESI) available. See DOI: 10.1039/c8mh00128f

‡ These authors contributed equally to this work.

delivery vehicle to load hydrophobic drugs through π - π stacking and hydrophobic interactions between GO and the drugs.¹¹⁻¹³ Photothermal-activated drug release can be achieved *in vitro* and *in vivo* by taking advantage of the near-infrared (NIR) light-mediated photothermal effect of GO resulting from its NIR optical absorption ability.¹⁴⁻¹⁷ However, its inefficient photothermal effect is the main obstacle for using GO as a drug delivery system or a PA imaging agent, attributed to the structural defects in the regular flat geometry of graphene introduced by oxidative processes. In comparison with the plasmonic photoacoustic contrast agents, such as gold nanorods, nanoshells, nanocages, nanostars, nanotriangles and nanovesicles, GO is hardly employed for PA imaging owing to its weak absorption in the NIR region and poor PA conversion efficiency resulting from its smaller sp^2 domains than graphene or reduced graphene oxide, greatly hindering its application in cancer theranostics.

Supramolecular chemistry is “chemistry beyond the molecule”, which is based upon intermolecular interactions, *i.e.* on the association of two or more building blocks being held together by non-covalent interactions.¹⁸ Different from traditional molecular chemistry that is predominantly based on covalent interactions, the reversible and dynamic nature of the non-covalent interactions endows the resultant supramolecular architectures with excellent stimuli-responsiveness and infinite possible applications in various fields.^{19,20} Bottom-up supramolecular assembly provides a productive tool to fabricate multifunctional hybrid systems by integrating individual functional components through non-covalent interactions. Among various non-covalent interactions, such as π - π stacking, hydrogen bonding, electrostatic interactions and charge-transfer interactions, host-guest molecular recognition is attracting more and more attention from scientists, arising from their distinctive properties by introducing macrocyclic hosts into the supramolecular systems.²¹⁻²⁸ Considering their highly symmetrical and rigid structures, sophisticated functionalization, and fruitful host-guest chemistry, pillar[n]arenes have become star molecules in supramolecular chemistry since 2008.^{29,30} Compared with other macrocyclic hosts, the easy functionalization and unique symmetrical structure of pillararenes have afforded them superior abilities to bind different guests and provided a useful platform for the fabrication of interesting supramolecular nanomaterials.³¹⁻³⁸ Fantastic supramolecular systems, such as liquid crystals, mechanical interlocking molecules, metal-organic frameworks, supramolecular polymers, drug delivery systems, cell imaging agents, transmembrane channels and cell glue, have been constructed by fully taking advantage of their unique properties.³⁹⁻⁴⁸ However, the development of functional hybrid materials exploiting the pillar[n]arene-based platforms has been scant until now.

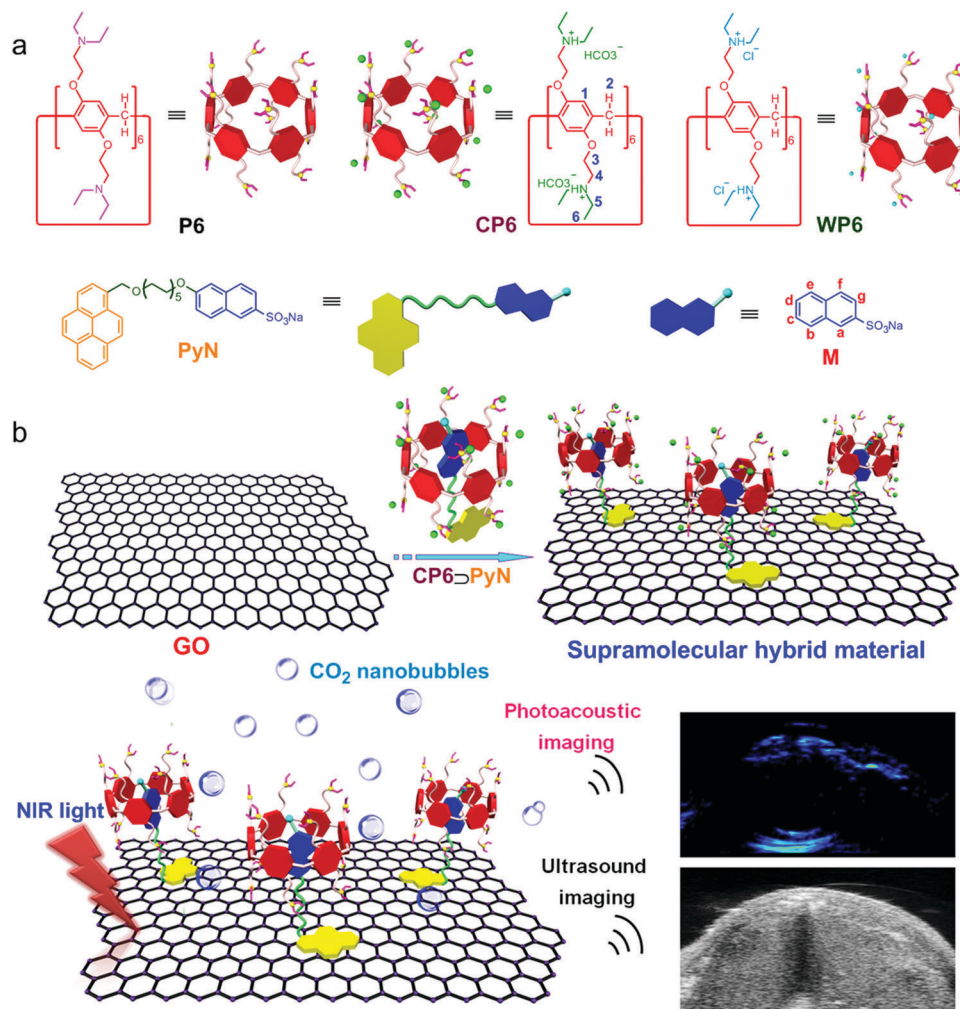
Herein, we report a novel strategy for preparing a supramolecular hybrid material (GO@CP6 \supset PyN) fabricated from GO and a pillar[6]arene-based host-guest complex by hierarchical self-assembly, which exhibited near-infrared (NIR) light-triggered PA and ultrasound (US) signal amplification (Scheme 1). For this purpose, a CO₂-responsive host-guest complex (CP6 \supset PyN) is constructed by using a pillar[6]arene CP6 containing 12 tertiary

amine groups as the host and an amphiphilic molecule PyN containing a pyrene tail as the guest. Driven by the π - π stacking between GO and the pyrene, and host-guest interactions between CP6 and PyN, CP6 \supset PyN is attached onto the surface of GO to form a hybrid material. The bicarbonate counterions on the surface of GO@CP6 \supset PyN are decomposed into carbon dioxide (CO₂) triggered by the NIR light-mediated photothermal effect of GO. *In vitro* and *in vivo* investigations demonstrated that the resultant CO₂ nanobubbles acting as “molecular boosters” can be used to significantly enhance the PA and US signals.

The neutral pillar[6]arene P6 was not able to interact with PyN in water due to its poor solubility and the shortage of driving forces. Host-guest complexation was achieved after the tertiary amine parts were changed into cationic tertiary ammonium groups upon protonation by CO₂. Multiple electrostatic interactions were responsible for the formation of the inclusion complex, which was demonstrated by ¹H NMR and 2D NOESY spectroscopies. Considering the poor solubility of PyN in water, sodium 2-naphthalenesulfonate (M) was employed as a model compound to study the host-guest complexation. The ¹H NMR spectrum of an equimolar solution of CP6 and M in D₂O exhibits only one set of peaks, suggesting that the complexation was rapidly exchanging on the ¹H NMR time scale (Fig. 1b). In comparison with the spectrum of free M (Fig. 1a), significant chemical shift changes were monitored for the resonances related to the protons on M, because these protons were threaded in the cavity and shielded by the electron-rich cyclic structure by the formation of CP6 \supset M. Additionally, the peaks corresponding to the protons on CP6 (H₁₋₆) shifted down-field upon formation of the host-guest complex, further confirming the interactions between CP6 and M. These observations indicated that the cavity of pillar[6]arene was large enough to wrap the guest molecule. 2D NOESY NMR spectroscopy was utilized to provide convincing insight into the formation of the host-guest inclusion complex. As shown in Fig. 1d, strong nuclear overhauser effect (NOE) correlations were detected between the peaks of the protons on M (H_{a-g}) and CP6 (H₁₋₆), demonstrating that the naphthalene ring penetrated into the cavity of the pillararene moiety, thus forming a 1:1 [2]pseudorotaxane-type host-guest complex.

The binding affinity (K_a) of CP6 \supset M was measured by isothermal titration calorimetry (ITC) investigation, where the K_a value of CP6 \supset M was determined to be $(1.43 \pm 0.22) \times 10^4 \text{ M}^{-1}$ in 1:1 complexation (Fig. 2). Meanwhile, some thermodynamic parameters (enthalpy and entropy changes, ΔH° and ΔS° , respectively) were obtained. As shown in Fig. 2, we determined that this complexation was primarily driven by the enthalpy change with entropic assistance ($T\Delta S > 0$; $\Delta H < 0$; $|\Delta H| > |T\Delta S|$).

Direct evidence for the formation of CP6 \supset PyN was obtained from conductivity tests and TEM investigations. The critical aggregation concentration of PyN was measured to be $2.43 \times 10^{-7} \text{ M}$ (Fig. S9, ESI[†]), and pronouncedly increased to $1.07 \times 10^{-6} \text{ M}$ in the presence of CP6 (Fig. S10, ESI[†]), ascribed to the host-guest complexation. As shown in the TEM images, the nanosheets self-assembled from PyN transformed into



Scheme 1 (a) Chemical structures of the building blocks (**P6**, **CP6**, **WP6**, **PyN** and **M**). (b) Schematic representation of the preparation of the supramolecular hybrid material (**GO@CP6>PyN**) exhibiting NIR light-triggered PA and US imaging enhancement.

nanoparticles by adding **CP6** caused by the host–guest interactions (Fig. S11, ESI[†]). The reason for the morphology changes of the self-assemblies was that the membrane curvature of the nanosheets became higher upon the insertion of **CP6** arising from the generation of electrostatic repulsion and steric hindrance.⁴⁹

GO@CP6>PyN hybrids were prepared by sonication of **CP6>PyN** (500 mg) in H₂O (100 mL) with 50 mg of GO for 4 h. After the sonication, the supernatant was dialyzed against H₂O to remove the excess amount of free **CP6>PyN** from the solution. Notably, the stability of the resultant supramolecular hybrid material was extremely high, and the homogeneous solution of **GO@CP6>PyN** could stand for more than 2 months without precipitation (Fig. S17, ESI[†]). In order to verify the successful preparation of **GO@CP6>PyN**, various characterizations were carried out, including atomic force microscopy (AFM), thermal gravimetric analysis (TGA), UV-vis and fluorescence titrations. The AFM image of **GO@CP6>PyN** shown in Fig. 3b indicated that the height of the supramolecular hybrid material was *ca.* 10.2 nm, apparently thicker than that of

pristine GO (1.18 nm, Fig. 3a). According to the molecular model, the length of **CP6>PyN** was calculated to be about 4.1 nm (Fig. S13, ESI[†]), approximately equal to half of the thickness changes of GO in the presence and absence of **CP6>PyN**. Driven by the π - π stacking interactions, the hydrophobic section containing the pyrenyl ring attached on the surfaces of GO to form **GO@CP6>PyN**, where the hydrophilic part containing the host–guest complex dispersed in the water. In the UV-vis spectrum of **GO@CP6>PyN**, the characteristic peaks at 325 and 341 nm ascribed to the pyrenyl group were recorded (Fig. 3c), further confirming the π -stacking of **CP6>PyN** to GO. Interestingly, a gradual increase in absorption in the range between 500 and 1000 nm was observed upon addition of **CP6>PyN** (Fig. S14, ESI[†]). This phenomenon was extremely conducive to improving the photothermal effect and PA signal of the resultant supramolecular hybrid material by increasing its light absorption efficiency. Fluorescence titration experiments were conducted to compare the difference in fluorescence emission between the solution of **CP6>PyN** and **GO@CP6>PyN**. Fig. 3d shows a broad emission band ranging

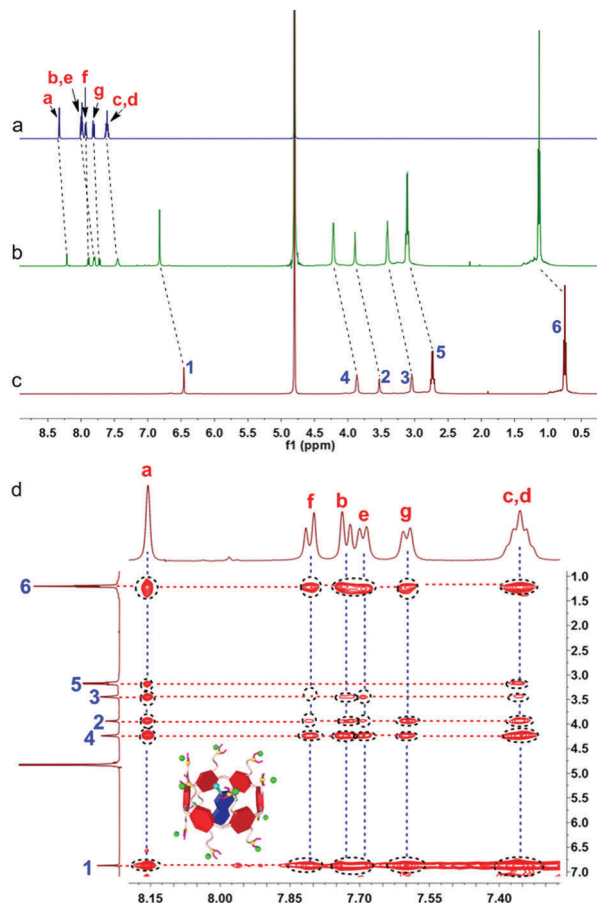


Fig. 1 ^1H NMR spectra (500 MHz, D_2O , 295 K) of (a) **M** (2.00 mM), (b) **CP6** (2.00 mM) and **M** (2.00 mM), and (c) **CP6** (2.00 mM). (d) 2D NOESY NMR spectrum (500 MHz, D_2O , 295 K) of **CP6** (10.0 mM) and **M** (10.0 mM).

from 425 to 650 nm, the characteristic emission of the pyrene excimer in aqueous solution. However, gradual addition of GO into the solution led to strong fluorescence quenching. This phenomenon was most likely caused by the fluorescence resonance energy transfer (FRET) effect, where **CP6** \supset **PyN** acted as a donor fluorophore and GO acted as the acceptor.^{50,51} By introducing the cationic host-guest complex into the hybrid material, the zeta potential value of GO increased from -37.4 to 8.7 mV (Fig. S15, ESI †). Moreover, the content of **CP6** \supset **PyN** in the supramolecular hybrid material was measured by TGA. TGA showed that the weight ratio between GO and **CP6** \supset **PyN** was 1:1 (Fig. S16, ESI †), indicating that the loading content was quite high. These data together strongly support the successful fabrication of **GO**@**CP6** \supset **PyN**.

To evaluate the photothermal properties of **GO**@**CP6** \supset **PyN**, different nanomaterials (**GO**, **CP6** \supset **PyN**, **GO**@**CP6** \supset **PyN**) were dispersed in water and then irradiated with a suitable laser (808 nm, 0.5 W cm^{-2}). The solution temperature was then monitored as a function of time (Fig. 3e). Negligible temperature change was detected for pure water. Upon laser illumination, the temperature of the **GO**@**CP6** \supset **PyN** solution increased from 25.4 to 63.3 $^\circ\text{C}$ within 3 min, in sharp contrast to the small temperature changes of the irradiated **GO** ($\Delta T = 20.5$ $^\circ\text{C}$) and

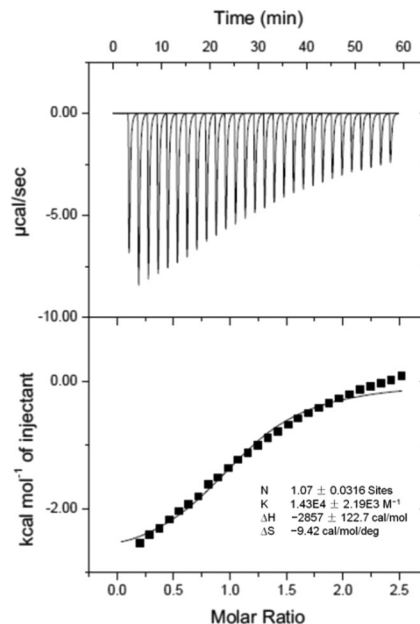


Fig. 2 Microcalorimetric titration of **M** with **CP6** in water at 298.15 K. Top: Raw ITC data for 27 sequential injections (10 μL per injection) of an **M** solution (2.00 mM) into a **CP6** solution (0.100 mM); bottom: net reaction heat obtained from the integration of the calorimetric traces.

CP6 \supset **PyN** ($\Delta T = 4.9$ $^\circ\text{C}$) samples. This temperature elevation of the **GO**@**CP6** \supset **PyN** solution was also confirmed by thermal images monitored using an IR camera, which showed a red color (**GO**@**CP6** \supset **PyN**) versus a blue color (pure water, Fig. 3e). Compared with that of **GO**, the temperature changes for **GO**@**CP6** \supset **PyN** were much more effective under the same conditions, demonstrating that the **GO**@**CP6** \supset **PyN** can rapidly and efficiently convert NIR light into thermal energy. The reason was that the absorbance of **GO**@**CP6** \supset **PyN** increased significantly compared with that of pristine **GO** (Fig. 3c and Fig. S14, ESI †), which was favorable to enhance its photothermal conversion efficiency, thus implying that **CP6** \supset **PyN** played a significant role in this supramolecular hybrid material. Meanwhile, when a **GO**@**CP6** \supset **PyN** aqueous solution at the same concentration was exposed to an 808 nm NIR laser at different power densities of 0.3, 0.5 and 1.0 W cm^{-2} for 3 min, an obvious laser power-dependent temperature increase was observed (Fig. 3f).

By taking advantage of the NIR light-mediated photothermal effect, **GO**@**CP6** \supset **PyN** can be used as a heat source to trigger the decomposition of the bicarbonate counterions, thus generating CO_2 nanobubbles. Therefore, we envisaged that **CP6** \supset **PyN** could act as a supramolecular chaperone to enhance the US and PA signals of the hybrid material. In order to monitor the release of CO_2 , we detected the weight loss of **GO**@**CP6** \supset **PyN** in the presence of NIR light irradiation at 808 nm for different times. During the experiments, we observed that the solution temperature increased to 82 $^\circ\text{C}$ after 10 min of irradiation. Fig. 3g verified the irradiation-dependent CO_2 release, and 76.8% of the bicarbonate counterions were decomposed upon NIR light irradiation for 10 min. The formed

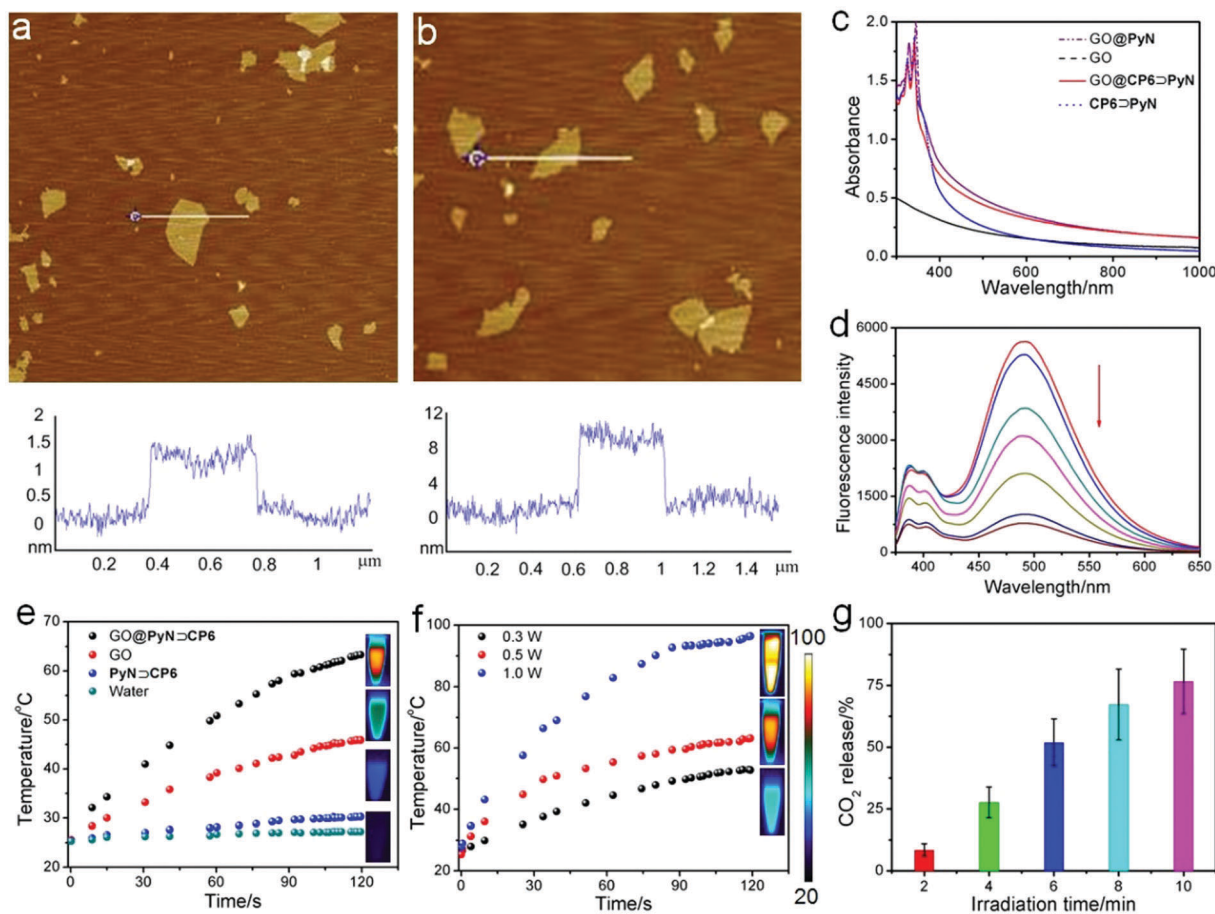


Fig. 3 AFM images of (a) GO and (b) GO@CP6-PyN. (c) UV-vis spectra of GO, CP6-PyN, GO@PyN and GO@CP6-PyN. (d) Fluorescence titration spectra of CP6-PyN (2 μM) in the presence of increasing GO. (e) The photothermal heating curves of pure water, CP6-PyN, GO and GO@CP6-PyN (the concentration of GO and CP6-PyN was $250 \mu\text{g mL}^{-1}$) under 808 nm laser irradiation at the power density of 0.5 W cm^{-2} . (f) The photothermal heating curves of GO@CP6-PyN under 808 nm laser irradiation at different power densities. (g) CO_2 release from GO@CP6-PyN upon laser irradiation for different time periods (808 nm, 0.5 W cm^{-2}).

nanobubbles were able to reflect and scatter ultrasound effectively (being echogenic), and could be utilized as contrast agents in diagnostic ultrasonography. Fig. 4b exhibited the 2D ultrasound images taken after 20 s of ultrasonication for the tube of water that was doped with CP6-PyN, GO, GO@WP6-PyN and GO@CP6-PyN, respectively. Compared with the other samples, considerable echo signals captured in the conventional B-mode were observed for the tube filled with an aqueous solution containing GO@CP6-PyN. Notably, the US signal arising from GO@WP6-PyN was much lower than that of GO@CP6-PyN. The only difference between them was located in the counter-anions of these hybrid materials, indicating that the generation of CO_2 was responsible for US resonance.

A preliminary evaluation of phantoms containing aqueous solutions of CP6-PyN, GO, or GO@WP6-PyN showed that they generated weak photoacoustic signal intensities (Fig. 4a). In sharp contrast, the PA signal produced by the sample of GO@CP6-PyN was much stronger at the same concentration. The PA signal intensity of GO@CP6-PyN was linearly correlated with its concentration ($R^2 = 0.99$). Additionally, the linear

slope of GO@CP6-PyN was markedly higher than those of the other groups (Fig. 4c), suggesting that GO@CP6-PyN can be a promising PA contrast agent. It is intriguing to find that an increase in PA intensity by a factor of *ca.* 4 was monitored upon NIR laser irradiation (Fig. 4d and Fig. S18–S22, ESI[†]). This phenomenon was not observed in the previous PA imaging studies. The reason for this PA enhancement might be the generation of CO_2 nanobubbles through the NIR light-mediated photothermal effect of GO, acting as nanoamplifiers to enhance the PA signal by increasing the vibration of the medium. In our case, GO@CP6-PyN possessed a stronger photothermal effect, so it is not surprising that the PA signal amplification by GO@CP6-PyN is remarkably higher than those of CP6-PyN, GO and GO@WP6-PyN.

Prior to the bio-relevant application of GO@CP6-PyN, its cytotoxicity was evaluated using a 3-(4',5'-dimethylthiazol-2'-yl)-2,5-diphenyl tetrazolium bromide (MTT) assay. As shown in Fig. S23 (ESI[†]), the relative cell viability in the presence of GO@CP6-PyN was higher than 80% even at a high concentration, confirming the excellent biocompatibility of this supra-molecular hybrid material. With the proof-of-concept imaging

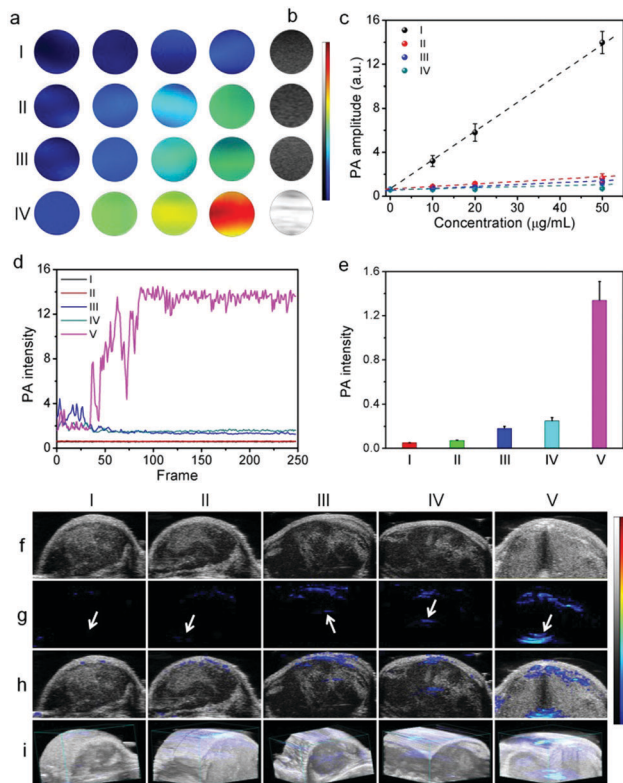


Fig. 4 (a) *In vitro* PA images, (b) US images, and (c) concentration-dependent PA intensity of (I) $\text{CP6} \supset \text{PyN}$, (II) GO, (III) $\text{GO@WP6} \supset \text{PyN}$, and (IV) $\text{GO@CP6} \supset \text{PyN}$. (d) PA spectra of (I) PBS, (II) $\text{CP6} \supset \text{PyN}$, (III) GO, (IV) $\text{GO@WP6} \supset \text{PyN}$, and (V) $\text{GO@CP6} \supset \text{PyN}$. *In vivo* (e) PA intensity, (f) 2D US images, (g) PA images, (h) merged images, and (i) 3D PA images of tumor tissues before and after the intratumoral administration of (I) PBS, (II) $\text{CP6} \supset \text{PyN}$, (III) GO, (IV) $\text{GO@WP6} \supset \text{PyN}$, and (V) $\text{GO@CP6} \supset \text{PyN}$. Arrows indicate the location of injections.

results in hand, *in vivo* experiments were conducted to verify the US and PA imaging capabilities of $\text{GO@CP6} \supset \text{PyN}$ using nude mice bearing U87MG tumors *via* intratumor injection ($250 \mu\text{g mL}^{-1}$, $20 \mu\text{L}$). Negligible US contrast enhancement in the tumor tissues was detected for the mice treated with GO, $\text{CP6} \supset \text{PyN}$ or $\text{GO@WP6} \supset \text{PyN}$ under B-mode (Fig. 4f). On the contrary, the US contrast of the tumor tissue for the mouse injected with $\text{GO@CP6} \supset \text{PyN}$ was brightened and the gray scale intensity increased effectively. Note that although the tumors were injected sporadically, the ultrasound signal is rather homogeneous throughout the tumor region, firmly demonstrating the excellent tissue permeability of the generated CO_2 nanobubbles arising from their small size. Like their micrometer-sized counterparts (microbubbles), these nanobubbles effectively reflected ultrasound, and were suitable contrast agents for US imaging. From the PA images (Fig. 4g), we found that the enhancement in PA signal was negligible for the mice injected with GO, $\text{CP6} \supset \text{PyN}$ or $\text{GO@WP6} \supset \text{PyN}$. In sharp contrast with these groups, the PA signal in the region of interest increased significantly for the tumors treated with $\text{GO@CP6} \supset \text{PyN}$, and was about 5.36, 7.44, and 18.9 times higher than those observed in the groups treated with

$\text{GO@WP6} \supset \text{PyN}$, GO, and $\text{CP6} \supset \text{PyN}$, respectively (Fig. 4e). Interestingly, the tertiary amine groups on the pillar[6]arene were able to be protonated by bubbling with CO_2 ,³⁸ and thus this supramolecular hybrid could be repeatedly used. These preliminary results suggest that our supramolecular hybrid material could be a promising candidate for US and PA imaging contrast enhancement, where the generated CO_2 nanobubbles act as “molecular boosters”.

Conclusions

In conclusion, we developed a novel supramolecular hybrid material, $\text{GO@CP6} \supset \text{PyN}$, integrating GO and a pillar[6]arene-based host-guest complex ($\text{CP6} \supset \text{PyN}$) driven by non-covalent interactions. By employing the NIR light-mediated photothermal effect of GO, the bicarbonate counterions on the surface of the supramolecular hybrid material were decomposed into CO_2 nanobubbles upon NIR laser irradiation. The generated CO_2 nanobubbles acting as “molecular boosters” can be used to enhance the US and PA signals, resulting from their small size and excellent tissue permeability. On the other hand, the supramolecular formulation effectively increased the NIR absorption of the resultant supramolecular hybrid material, improving the photothermal effect of $\text{GO@CP6} \supset \text{PyN}$, which was further beneficial to the enhancement of its PA signal. This supramolecular method provides an exceedingly exquisite strategy to improve the PA and US performances of functional hybrid materials by fully taking advantage of supramolecular chemistry, which paves a distinctive way to develop smart nanomaterials for imaging-guided theranostic applications.

Author contributions

G. Yu, Z. Mao, F. Huang and X. Chen conceived and designed the research. X. Fu conducted the AFM measurements. J. Yang and L. Shao performed the ^1H NMR and 2D NOESY studies. Z. Wang, Y. Liu and Z. Yang carried out the PA imaging. Z. Mao performed the TGA studies. G. Yu, F. Zhang, W. Fan, J. Song and Z. Zhou analysed the data. G. Yu, Z. Mao, C. Gao, F. Huang and X. Chen co-wrote the paper.

Conflicts of interest

There are no conflicts to declare.

Acknowledgements

This work was supported by the Intramural Research Program of the National Institute of Biomedical Imaging and Bioengineering, and National Institutes of Health (ZIA EB000073), the National Natural Science Foundation of China (21674091, 21434005, 91527301), the National Basic Research Program (2013CB834502), the Zhejiang Provincial Natural Science Foundation of China (Grant LR16E030001), and the Open Project of State Key Laboratory of Supramolecular Structure and Materials.

Notes and references

- 1 H. F. Zhang, K. Maslov, G. Stoica and L. V. Wang, *Nat. Biotechnol.*, 2006, **24**, 848–851.
- 2 K. Pu, A. J. Shuhendler, J. V. Jokerst, J. Mei, S. S. Gambhir, Z. Bao and J. Rao, *Nat. Nanotechnol.*, 2014, **9**, 233–239.
- 3 H. Li, P. Zhang, L. P. Smaga, R. A. Hoffman and J. Chan, *J. Am. Chem. Soc.*, 2015, **137**, 15628–15631.
- 4 Y.-S. Chen, W. Frey, S. Kim, P. Kruizinga, K. Homan and S. Emelianov, *Nano Lett.*, 2011, **11**, 348–354.
- 5 Y. Shi, H. Qin, S. Yang and D. Xing, *Nano Res.*, 2016, **9**, 3644–3655.
- 6 Q. Miao and K. Pu, *Bioconjugate Chem.*, 2016, **27**, 2808–2823.
- 7 K. Yang, S. Zhang, G. Zhang, X. Sun, S.-T. Lee and Z. Liu, *Nano Lett.*, 2010, **10**, 3318–3323.
- 8 W. Li, J. Wang, J. Ren and X. Qu, *Adv. Mater.*, 2013, **25**, 6737–6743.
- 9 C. Chung, Y.-K. Kim, D. Shin, S.-R. Ryoo, B. H. Hong and D.-H. Min, *Acc. Chem. Res.*, 2013, **46**, 2211–2224.
- 10 H. Zhang, G. Grüner and Y. Zhao, *J. Mater. Chem. B*, 2013, **1**, 2542–2567.
- 11 L. Zhang, J. Xia, Q. Zhao, L. Liu and Z. Zhang, *Small*, 2010, **6**, 537–544.
- 12 J. T. Robinson, S. M. Tabakman, Y. Liang, H. Wang, H. S. Casalongue, D. Vinh and H. Dai, *J. Am. Chem. Soc.*, 2011, **133**, 6825–6831.
- 13 Y. Yang, Y.-M. Zhang, Y. Chen, D. Zhao, J.-T. Chen and Y. Liu, *Chem. – Eur. J.*, 2012, **18**, 4208–4215.
- 14 H. Kim, D. Lee, J. Kim, T. Kim and W. J. Kim, *ACS Nano*, 2013, **7**, 6735–6746.
- 15 W. Miao, G. Shim, S. Lee, S. Lee, Y. S. Choe and Y.-K. Oh, *Biomaterials*, 2013, **34**, 3402–3410.
- 16 V. Shanmugam, S. Selvakumar and C.-S. Yeh, *Chem. Soc. Rev.*, 2014, **43**, 6254–6287.
- 17 J. Song, X. Yang, O. Jacobson, L. Lin, P. Huang, G. Niu, Q. Ma and X. Chen, *ACS Nano*, 2015, **9**, 9199–9209.
- 18 M. C. T. Fyfe and J. F. Stoddart, *Acc. Chem. Res.*, 1997, **30**, 393–401.
- 19 J.-M. Lehn, *Chem. Soc. Rev.*, 2007, **36**, 151–160.
- 20 X. Zhang and C. Wang, *Chem. Soc. Rev.*, 2011, **40**, 94–101.
- 21 Q.-C. Wang, D.-H. Qu, J. Ren, K. Chen and H. Tian, *Angew. Chem., Int. Ed.*, 2004, **43**, 2661–2665.
- 22 Y. J. Jeon, H. Kim, S. Jon, N. Selvapalam, D. H. Seo, I. Oh, C.-S. Park, S. R. Jung, D.-S. Koh and K. Kim, *J. Am. Chem. Soc.*, 2004, **126**, 15944–15945.
- 23 W.-H. Huang, P. Y. Zavalij and L. Isaacs, *Angew. Chem., Int. Ed.*, 2007, **46**, 7425–7427.
- 24 Z. Niu and H. W. Gibson, *Chem. Rev.*, 2009, **109**, 6024–6046.
- 25 W. Jiang, A. Schäfer, P. C. Mohr and C. A. Schalley, *J. Am. Chem. Soc.*, 2010, **132**, 2309–2320.
- 26 K. Zhu, V. N. Vukotic and S. J. Loeb, *Angew. Chem., Int. Ed.*, 2012, **51**, 2168–2172.
- 27 D.-S. Guo and Y. Liu, *Chem. Soc. Rev.*, 2012, **41**, 5907–5921.
- 28 Y. Lan, X. J. Loh, J. Geng, Z. Walsh and O. A. Scherman, *Chem. Commun.*, 2012, **48**, 8757–8759.
- 29 T. Ogoshi, S. Kanai, S. Fujinami, T. A. Yamagishi and Y. Nakamoto, *J. Am. Chem. Soc.*, 2008, **130**, 5022–5023.
- 30 T. Ogoshi, T.-a. Yamagishi and Y. Nakamoto, *Chem. Rev.*, 2016, **116**, 7937–8002.
- 31 W. Cui, H. Tang, L. Xu, L. Wang, H. Meier and D. Cao, *Macromol. Rapid Commun.*, 2017, **38**, 1700161.
- 32 N. Song, D.-X. Chen, M.-C. Xia, X.-L. Qiu, K. Ma, B. Xu, W. Tian and Y.-W. Yang, *Chem. Commun.*, 2015, **51**, 5526–5529.
- 33 W. Wang, L.-J. Chen, X.-Q. Wang, B. Sun, X. Li, Y. Zhang, J. Shi, Y. Yu, L. Zhang, M. Liu and H.-B. Yang, *Proc. Natl. Acad. Sci. U. S. A.*, 2015, **112**, 5597–5601.
- 34 L. Luo, G. Nie, D. Tian, H. Deng, L. Jiang and H. Li, *Angew. Chem., Int. Ed.*, 2016, **55**, 12713–12716.
- 35 J. Murray, K. Kim, T. Ogoshi, W. Yao and B. C. Gibb, *Chem. Soc. Rev.*, 2017, **46**, 2479–2496.
- 36 B. Cheng and A. E. Kaifer, *J. Am. Chem. Soc.*, 2015, **137**, 9788–9791.
- 37 M. Guo, X. Wang, C. Zhan, P. Demay-Drouhard, W. Li, K. Du, M. A. Olson, H. Zuillhof and A. C.-H. Sue, *J. Am. Chem. Soc.*, 2018, **140**, 74–77.
- 38 K. Jie, Y. Zhou, Y. Yao, B. Shi and F. Huang, *J. Am. Chem. Soc.*, 2015, **137**, 10472–10475.
- 39 D. R. Cao, Y. H. Kou, J. Q. Liang, Z. Z. Chen, L. Y. Wang and H. Meier, *Angew. Chem., Int. Ed.*, 2009, **48**, 9721–9723.
- 40 N. L. Strutt, R. S. Forgan, J. M. Spruell, Y. Y. Botros and J. F. Stoddart, *J. Am. Chem. Soc.*, 2011, **133**, 5668–5671.
- 41 W. Si, L. Chen, X.-B. Hu, G. Tang, Z. Chen, J.-L. Hou and Z.-T. Li, *Angew. Chem., Int. Ed.*, 2011, **50**, 12564–12568.
- 42 Q. Duan, Y. Cao, Y. Li, X. Hu, T. Xiao, C. Lin, Y. Pan and L. Wang, *J. Am. Chem. Soc.*, 2013, **135**, 10542–10549.
- 43 X. Wang, K. Han, J. Li, X. Jia and C. Li, *Polym. Chem.*, 2013, **4**, 3998–4003.
- 44 H. Zhang, X. Ma, K. T. Nguyen and Y. Zhao, *ACS Nano*, 2013, **7**, 7853–7863.
- 45 L.-L. Tan, H. Li, Y. Tao, S. X.-A. Zhang, B. Wang and Y.-W. Yang, *Adv. Mater.*, 2014, **26**, 7027–7031.
- 46 Y. Sun, F. Guo, L. Zuo, J. Hua and G. Diao, *Nat. Commun.*, 2016, **7**, 12042.
- 47 G. Yu, B. C. Yung, Z. Zhou, Z. Mao and X. Chen, *ACS Nano*, 2018, **12**, 7–12.
- 48 R. Wang, Y. Sun, F. Zhang, M. Song, D. Tian and H. Li, *Angew. Chem., Int. Ed.*, 2017, **56**, 5294–5298.
- 49 G. Yu, X. Zhou, Z. Zhang, C. Han, Z. Mao, C. Gao and F. Huang, *J. Am. Chem. Soc.*, 2012, **134**, 19489–19497.
- 50 G. Yu, M. Xue, Z. Zhang, J. Li, C. Han and F. Huang, *J. Am. Chem. Soc.*, 2012, **134**, 13248–13251.
- 51 H.-L. Zhang, X.-L. Wei, Y. Zang, J.-Y. Cao, S. Liu, X.-P. He, Q. Chen, Y.-T. Long, J. Li, G.-R. Chen and K. Chen, *Adv. Mater.*, 2013, **25**, 4097–4101.